Burns & Trauma, 2026, **14**, tkag007
https://doi.org/10.1093/burnst/tkag007
Advance access publication date 15 January 2026
Research Article

Negative pressure-induced fibroblast activation for wound healing through the Piezo1-Ca^{2+}-NFAT3 signaling pathway

Shu-Ao Xiao[1,‡], Ni Liu[2,‡], Yi-Wei Cui[3,‡], Hang Li[4], Yu-Chen Dong[3], Jie-Zhang Tang[3], Hao Zhang[5], Wen-Xuan Wang[6], Yong-Qian Bian[3,*], Jing Li[3,*], Xue-Yong Li[4,*]

[1]Department of Plastic Surgery, Xijing Hospital, Fourth Military Medical University, No. 127, Changle West Road, Xincheng District, Xi'an, Shaanxi, 710032, China
[2]Department of Pain Management, the First Affiliated Hospital of Xi'an Jiaotong University, No. 277, Yanta West Road, Yanta District, Xi'an, Shaanxi, 710061, China
[3]Department of Burn and Plastic Surgery, Tangdu Hospital, Fourth Military Medical University, No. 1, Xinsi Road, Baqiao District, Xi'an, Shaanxi, 710000, China
[4]Department of Burn, Plastic and Wound Repair Surgery, the Second Affiliated Hospital, Xi 'an Jiaotong University, No. 157, West Fifth Road, Xincheng District, Xi'an, Shaanxi, 710004, China
[5]Department of Burn and Plastic Surgery, the 927th Hospital of the Joint Logistic Support Force, No. 3, Yushui Road, Nanping Town, Simao District, Pu'er, Yunnan, 665000, China
[6]Burn and Dermatology Surgery, Xijing Hospital, Fourth Military Medical University, No. 127, Changle West Road, Xincheng District, Xi'an, Shaanxi, 710032, China

*Corresponding authors. Xue-Yong Li, E-mail: lixueyong641123@163.com; Jing Li, E-mail: lijing02@fmmu.edu.cn; Yong-Qian Bian, yongqianbian@163.com.

‡Shu-Ao Xiao, Ni Liu, and Yi-Wei Cui contributed equally to this work.

Abstract

Background: Negative pressure wound therapy (NPWT) is widely used to promote wound healing, yet the mechanotransduction mechanisms underlying its efficacy remain unclear because of the absence of precise and controllable *in vitro* negative pressure loading devices for cellular-level studies. Therefore, this study aims to develop a precise and controllable *in vitro* negative pressure loading device and to elucidate the mechanotransduction mechanism by which negative pressure activates dermal fibroblasts during wound healing.

Methods: We developed a high-precision negative pressure loading device compatible with six-well plates, facilitating independent and intelligent control over negative pressure values, durations, and modes for each well. To validate the uniformity and stability of the negative pressure environment, finite element analysis (FEA) was implemented. The mechanism was explored using proteomic profiling of negative pressure-treated fibroblasts, complemented by molecular interrogation of Piezo1 expression and calcium signaling dynamics. The results of functional studies integrated genetic silencing and pharmacological modulation of the pathway, with *in vivo* confirmation through SD rat-based NPWT experiments.

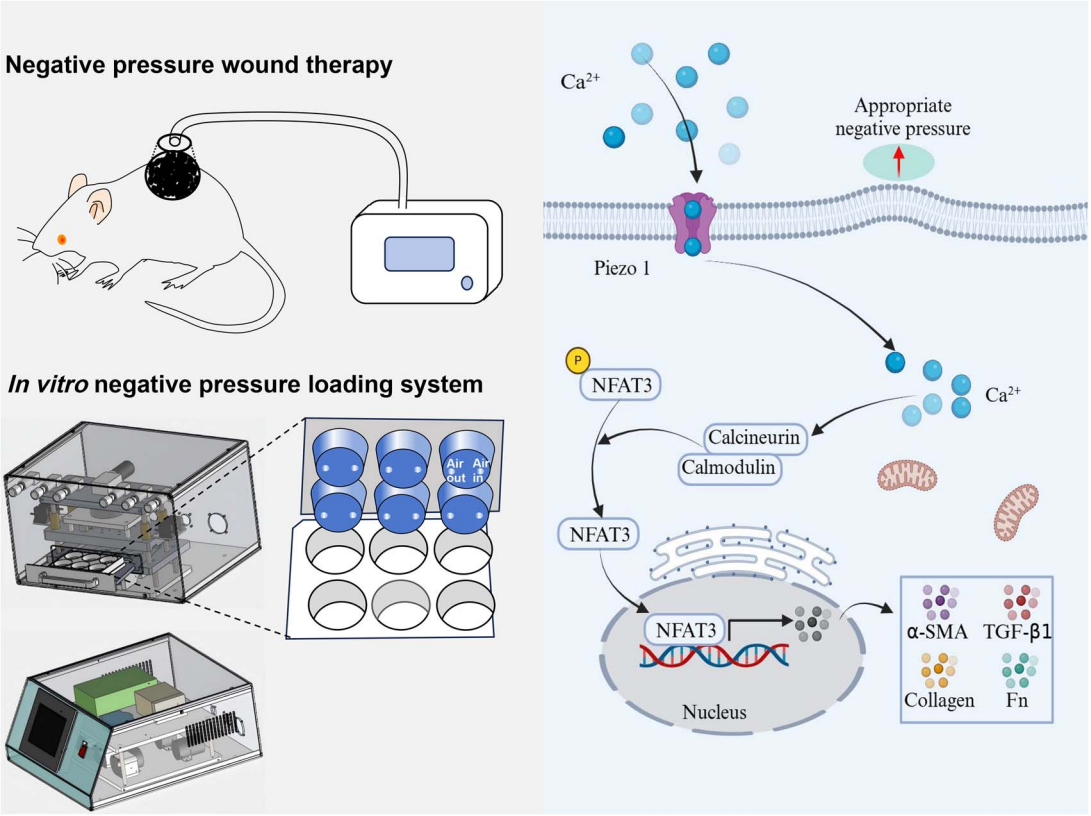
Results: FEA confirmed a stable pressure distribution within the negative pressure chamber. The cells experienced predominantly compressive stresses that scaled linearly with the applied pressure, reaching −2 kPa at −40 mmHg. We found that applying a continuous negative pressure of −40 mmHg for 2 hours significantly activated dermal fibroblasts. TMT-based proteomic analysis revealed the upregulation of Piezo1 in negative pressure-treated dermal fibroblasts, which was further confirmed by molecular and immunohistochemical analyses of both cellular and granulation tissue samples. Pharmacological inhibition or knockdown of Piezo1 attenuated negative pressure-induced dermal fibroblast activation *in vivo* and *in vitro*. Mechanistically, we determined that Piezo1-mediated Ca^{2+} influx and the calcineurin/NFAT3 signaling pathway are critically enhanced during this process.

Conclusions: This study revealed that the Piezo1-Ca^{2+}-NFAT3 mechanotransduction axis is the central pathway that mediates the therapeutic effects of NPWT. This work lays the foundational groundwork for elucidating the biomechanical mechanisms of negative pressure and reveals new approaches for research in tissue engineering and regenerative medicine.

Received: May 29, 2025. **Revised:** January 7, 2026. **Accepted:** January 8, 2026
© The Author(s) 2026. Published by Oxford University Press.
This is an Open Access article distributed under the terms of the Creative Commons Attribution-NonCommercial License (https://creativecommons.org/licenses/by-nc/4.0/), which permits non-commercial re-use, distribution, and reproduction in any medium, provided the original work is properly cited. For commercial re-use, please contact reprints@oup.com for reprints and translation rights for reprints. All other permissions can be obtained through our RightsLink service via the Permissions link on the article page on our site—for further information please contact journals.permissions@oup.com.

Downloaded from academic.oup.com/burnstrauma/article/doi/10.1093/burnst/tkag007/8426274 by guest on 12 October 2026

Graphical Abstract



Keywords: Negative pressure wound therapy; Finite element analysis; Fibroblasts; Piezo1; calcineurin/NFAT signaling pathway; Wound healing

Highlights

- Pioneered a six-channel automated *in vitro* negative pressure loading system for precise mechanical stimulation.
- Established finite element modeling to quantify cellular mechanical responses under negative pressure.
- Identified optimal parameters (–40 mmHg, 2 kPa, 2 h) for enhanced fibroblast activation via negative pressure stimuli.
- Unveiled Piezo1 as the unique mechanosensor governing negative pressure-induced fibroblast activation.
- Disclosed the novel Piezo1/Calcineurin/NFAT3 mechanotransduction cascade in mechanical regulation of fibroblast function.

Background

Negative pressure wound therapy (NPWT) has attracted significant attention in recent decades because of its reproducible clinical benefits in promoting wound healing [1]. In practice, NPWT acts through a combination of mechanisms, including continuous removal of exudate, reduction of tissue edema, maintenance of a moist and stable wound microenvironment, improvement of local perfusion, and mechanical deformation of wound tissues/cells that can trigger reparative responses [2]. These effects act in concert to enable wound healing. However, compared with the well-recognized roles of exudate drainage and microcirculatory improvement *in vivo*, the cellular and molecular responses to isolated negative pressure stimulation remain incompletely understood because most existing studies have been performed at the animal or clinical level rather than under controlled *in vitro* conditions [3, 4].

To investigate these biochemical effects, developing effective *in vitro* negative pressure loading devices is essential. However, existing *in vitro* negative pressure loading devices are often simple and typically consist of a sealed chamber connected to a vacuum pump or drainage bottle, which leads to imprecise pressure levels and inadequate growth conditions [5–9]. Consequently, there is an urgent need for more sophisticated and precise *in vitro* negative pressure loading devices to enable rigorous mechanistic studies.

Finite element analysis (FEA) is a powerful numerical method used to solve complex engineering problems by discretizing intricate structures into smaller elements for detailed behavioral analysis [10]. In biomedical research, FEA facilitates the simulation of cellular responses to various mechanical environments. For instance, Jakka et al. utilized FEA to examine the mechanical interactions of endothelial cells within vascular structures [11]. Given the complexity of mechanical conditions in negative pressure environments, FEA can better capture the dynamics of gas flow, stress distribution, and cell–substrate interactions, offering a realistic representation of the mechanical environment experienced by cells [12]. However, studies validating the efficacy of negative pressure environments remain scarce.

Mechanotransduction—the process of converting mechanical forces into biochemical signals—plays a pivotal role in understanding cellular behavior under negative pressure [13].

Downloaded from academic.oup.com/burnstrauma/article/doi/10.1093/burnst/tkag007/8426274 by guest on 12 October 2026

Negative pressure has been shown to induce phenotypic changes in various cell types. For instance, it enhances keratinocyte migration by increasing intracellular calcium levels [14] and activates endothelial cells towards a migratory and proliferative phenotype [15]. Notably, several studies have reported that negative pressure can promote dermal fibroblast activation in three-dimensional cultures [16–19]. However, the mechanical environment in such settings is highly complex and involves shear forces, tensile stresses, and negative pressure, making isolation of the specific effects of negative pressure alone difficult. Moreover, the mechanotransductive pathways underlying dermal fibroblast activation in response to negative pressure have yet to be elucidated.

In this study, we developed a novel, controllable *in vitro* negative pressure loading device compatible with six-well plates, enabling precise manipulation of negative pressure levels, durations, and modes. Using FEA, we validated the efficacy of the device in simulating the negative pressure environment. Proteomic analysis and subsequent biochemical experiments revealed that Piezo1 is a critical mechanosensor that mediates the negative pressure-induced activation of dermal fibroblast through the calcineurin/NFAT3 signaling pathway. This research provides not only a robust platform for advancing negative pressure biomechanics but also new insights for tissue engineering and regenerative medicine applications.

Methods

Research and application of *in vitro* negative pressure loading devices

The device we developed is composed of two main components: an negative pressure regulation module (housed within the incubator) and an intelligent control system (positioned outside the incubator). The negative pressure regulation module consists of six negative pressure suction cups, each corresponding to a well in a six-well plate. Specifically, each negative pressure suction cup is equipped with a sealing system, an negative pressure suction pipeline, an negative pressure sensor, and an inlet pipeline. The inlet pipeline is further integrated with a gas microflow sensor and a precision flow control valve. Upon placement of a six-well plate into the device, the sealing system pressurizes and isolates each well into an independent sealed chamber. An negative pressure pump is then activated to continuously extract air from these chambers, thereby creating a controlled negative pressure environment. Simultaneously, the gas microflow sensor and precision flow control valve within the inlet pipeline dynamically regulate the negative pressure magnitude within each chamber. The intelligent control system, which is located outside the incubator, includes a variable-speed vacuum pump, electrical circuitry, and a high-precision signal acquisition module. These components enable real-time monitoring of the negative pressure intensity and gas flow rates within each chamber. Additionally, the system supports automated selection and adjustment of experimental parameters—such as negative pressure values, cycle durations, and negative pressure application modes—through an intuitive touchscreen interface. This design allows for independent configurations of negative pressure values and modes for each well, accommodating diverse experimental requirements with high precision and flexibility. Schematics of the partial devices are shown in Supplementary Fig. S1. An additional movie file shows the devices in more detail (see Supplementary video 1).

Finite element analysis

Geometric modeling

Each individual negative pressure chamber was modeled as a cylindrical enclosure (diameter 35 mm, height 30 mm) according to the actual negative pressure loading device. The base of the six-well plate was assigned a thickness of 1 mm, and the inlet/outlet ports (diameter 4 mm) were positioned symmetrically on both sides of the central axis. A fixing frame surrounding the plate was included to reproduce the clamping condition. The sealing gasket was modeled as silicone rubber (cross-section 3 mm, width 5 mm) at a 1:1 scale to ensure consistency with the experimental setup.

Finite element mesh generation

The geometric model was imported into ANSYS ICEM CFD for three-dimensional mesh generation across different regions. A multidomain meshing strategy was used: solid structures (culture plate, clamp, and cell layer) were discretized with tetrahedral elements, whereas the gas/liquid chamber domains were meshed with structured hexahedral elements to better capture pressure gradients. Local mesh refinement was applied at the chamber bottom, around the inlet/outlet ports, and at the cell–dish interface to improve the solution accuracy in high-stress/pressure regions. The final mesh comprised 2 345 234 nodes, 327 529 tetrahedral elements, and 12 098 hexahedral elements, and mesh conformity was ensured by sharing common nodes between adjacent parts. The mesh was then exported in BDF format and imported into COMSOL 6.0 for assignment of material properties, boundary conditions, and subsequent FEA.

Material parameter settings

A linear elastic constitutive model was applied to both the culture plate and the cellular structures. The culture plate was assigned an elastic modulus of 930 kPa, a tensile strength of 1000 mPa, and a Poisson's ratio of 0.45. The modeled cells, $\sim$20 μm in size, were characterized by an elastic modulus of 8.04 ± 0.12 kPa and a Poisson's ratio of 0.49. The culture medium consisted of low-glucose Dulbecco's modified Eagle's medium (DMEM) supplemented with 10% serum, with 2.5 mL of medium per well. The medium had a density of 1.05 g/cm^3 and a dynamic viscosity of 1 mPa·s. Air was defined as having a density of 1.29 kg/m^3 and a dynamic viscosity of 0.001 mPa·s. Given that the density and viscosity of the culture medium closely approximate those of water, water-related parameters were used as reference values where appropriate. To represent a confluent monolayer, the cell layer was additionally modeled as a 5 μm isotropic continuous film bonded to the dish surface to ensure efficient load transfer.

Boundary condition settings

To reproduce the actual mechanical constraint of the device, nodes along the outer rim of the culture plate were constrained in the vertical (Z) direction while allowing limited in-plane deformation, corresponding to a simply supported clamping state. Negative pressure was applied at the extraction port, and the inlet port was set to atmospheric pressure to generate a difference in working pressure. The upper surface in contact with the medium was defined as a free boundary, whereas the lateral boundaries were maintained at zero pressure. For the

Downloaded from academic.oup.com/burnstrauma/article/doi/10.1093/burnst/tkag007/8426274 by guest on 12 October 2026

cellular structures, the bottom nodes at the cell–dish interface were defined as bonded to mimic firm adhesion, and all other cell surfaces were set as free boundaries to allow deformation under negative pressure loading.

Fundamental principles and governing equations

The basic governing equations for fluid and solid analysis are detailed in the Supplementary material.

Preparation of rat primary dermal fibroblasts

Dorsal skin samples were harvested from neonatal rats within 3 days of birth. After thorough disinfection, the connective tissue was carefully removed, and the skin was cut into ~1 mm^3 pieces. The tissue fragments were seeded into cell culture flasks with a minimal volume of complete medium, consisting of 10% fetal bovine serum and 1% penicillin–streptomycin solution, to ensure that the tissue pieces were fully immersed. Once the tissue adhered to the flask surface, additional complete medium was added, and the cultures were maintained in a 5% CO_2 incubator at 37°C. The medium was replaced, and the cells were passaged at regular intervals on the basis of their growth status. All experiments were performed using dermal fibroblasts at passages 3–5, and within each independent experiment, the treatment and control groups were derived from cells of the same passage.

Cell Counting Kit-8 assay

Fibroblasts were prepared as a cell suspension and seeded into six-well plates at a density of 1.5×10^5 cells per well. After overnight incubation to allow for cell attachment and normal growth, the cells in each well were divided into six groups—0, −10, −20, −30, −40, and − 50 mmHg—and subjected to 1 hour of negative pressure stimulation. Alternatively, the cells were exposed to −40 mmHg negative pressure for 0, 1, 2, 3, 4, or 5 hours for a total of six groups. The plates were then placed in the *in vitro* negative pressure device, and the corresponding negative pressure conditions were applied, followed by normal culture for 24 hours. After the culture medium was removed, 1 mL of DMEM and 100 μL of Cell Counting Kit-8 (CCK-8) reagent were added to each well, and the plates were incubated for 1 hour. Afterward, 100 μL of the supernatant from each well was transferred to a 96-well plate, with six replicate wells per condition. Blank wells containing only 100 μL of DMEM were used as controls. The absorbance (OD value) of each sample was measured at 450 nm, and the mean values were calculated.

Western blot analysis

After the cells were cultured for 24 hours under specific experimental conditions, the supernatant was collected and removed from the culture medium. For immunoblotting, the cells were lysed on ice for 30 minutes in radioimmunoprecipitation assay (RIPA) buffer (Beyotime) supplemented with protease and phosphatase inhibitors. The lysates were then centrifuged at 12000 × g for 20 minutes at 4°C. The supernatant was carefully transferred to a new tube, and the protein concentration was quantified using a BCA protein assay kit (Thermo Fisher Scientific, USA). The protein samples were mixed with loading buffer (Beyotime) and heated at 100°C for 5 minutes to achieve complete denaturation. The proteins were subsequently separated by SDS–polyacrylamide gel electrophoresis (SDS–PAGE) and transferred onto a polyvinylidene difluoride (PVDF) membrane. The membrane was blocked with 5% bovine serum albumin in Tris-buffered saline with Tween 20 (TBST) for 1 hour, followed by incubation with primary antibodies overnight at 4°C and secondary antibodies at room temperature for 1 hour. Protein signals were detected and documented using an appropriate imaging system.

The primary antibodies used were as follows: anti-Piezo1 (ab128245, 1:1000 dilution, 287 kDa), α-smooth muscle actin (α-SMA) (14395–1-AP, 1:4000 dilution, 42 kDa), TGF-β1 (ab215715, 1:1000 dilution, 44 kDa), Collagen I (14695–1-AP, 1:2000 dilution, 130 kDa), Fibronectin (Fn) (ab2413, 1:500 dilution, 285 kDa), PCNA (60097–1-ig, 1:10000 dilution, 36 kDa), calcineurin (CaN) (ab109412, 1:10000 dilution, 58 kDa), calmodulin (CALM) (10541–1-AP, 1:1000 dilution, 17 kDa), NFAT1 (22023–1-AP, 1:2000 dilution, 135 kDa), NFAT2 (66963–1-Ig, 1:2000 dilution, 101 kDa), NFAT3 (bs-6461R, 1:1000 dilution, 95 kDa), NFAT4 (18222–1-AP, 1:2000 dilution, 116 kDa), p-NFAT3 (AF7389, 1:1000 dilution, 95 kDa), H3 histone (ab186742, 1:1000 dilution, 17 kDa), GAPDH (60004–1-ig, 1:10000 dilution, 37 kDa), and β-tubulin (10094–1-AP, 1:6000, 50 kDa).

Quantitative real-time PCR

Total RNA was extracted from cells with TRIzol reagent (Ambion Life Technologies, USA) for quantitative analysis of mRNA expression levels. The concentration of the extracted RNA was measured, followed by reverse transcription using a cDNA synthesis kit (Takara, Japan). In the quantitative real time (qPCR) analysis, the resulting cDNA served as the template. The reaction setup was prepared according to the PCR kit specifications, and amplification was performed with the CFX Connect™ system. The primers used in our study were as follows:

Gene name	Forward primer	Reverse primer
Piezo1	CGGACAGTGAGGAG-GAAGAGGAG	CCTGTTCACGACGCT-GCCTTAG
Snx9	ATGGCCCTAT-GTGGGTTTATC	AGGAGACGTTCATA TAACCAGTC
Dbn1	CAACTGGGTTGGT-GAGGAT	TGCTGGCATTCA-CAATTAC
Myadm	GGTGAGATCACTGGC-TACATGG	TCACTGATGAAG-GCAAAGAT
GAPDH	CTTCTCTTGTGA-CAAAGTGGACAT	CTTGCCGTGGGTA-GAGTCAT

Immunofluorescence

The cell samples were fixed in 4% paraformaldehyde (PFA) for 15 minutes at room temperature, and the granulation tissue samples were fixed overnight in the same solution. Following fixation, tissue samples were subjected to embedding, freezing, and sectioning procedures. Both cell and tissue samples were washed, permeabilized, and blocked prior to for staining. Specific protein expression was analyzed using the following primary antibodies: anti-Piezo1 (Abcam, ab128245, 1:100), anti-Ki67 (CST, #9449, 1:400), anti-F-actin (Abcam, ab130935, 1:500), anti-α-SMA (14395–1-AP, 1:400), and NFAT3 (bs-6461R, 1:100).

Calcium imaging

Dermal fibroblasts were seeded into six-well plates and incubated overnight. The following day, the cells were cultured

Downloaded from academic.oup.com/burnstrauma/article/doi/10.1093/burnst/tkag007/8426274 by guest on 12 October 2026

for 2 hours under an negative pressure of ∼−40 mmHg. Fluo-3 AM was added to the culture medium at a final concentration of 10 μmol/L and incubated in the dark for 30 minutes to allow for intracellular loading. DAPI was used to stain the cell nuclei for visualization. After the samples were sealed with an anti-fluorescence quenching agent, images were captured using a fluorescence microscope, and the fluorescence intensity was quantified.

Cell transfection and inhibition

For Piezo1 silencing, dermal fibroblasts were transfected with siRNAs using Lipofectamine™ 2000 (Thermo Fisher Scientific, USA) following the manufacturer's protocol. The targeted sequence of the siRNA directly targeting rat Piezo1 RNA was 5′-CGGCCAACAUAAAGAACAUTT. The negative control was a scrambled siRNA (5′-UUCUCCGAACGUGUCACGUTT).

For pharmacological inhibition, the Piezo1 inhibitor GsMTx-4 (Alomone Labs, Jerusalem, Israel) was dissolved in PBS. In accordance with previous studies, a concentration of 5 μM GsMTx-4 was used in all the experiments. Additionally, cyclosporin A (CsA, 10 μM; MCE, 59865-13-3; Shanghai, China), the TRPV4 inhibitor GSK2193874 (3 nM; MCE, 1336960-13-4) and the Ca^{2+} chelator BAPTA-AM (10 μM; MCE, 126150-97-8) were used to inhibit calcineurin activity, block TRPV4, and chelate intracellular Ca^{2+}, respectively.

Animal models

Twenty-four male Sprague–Dawley (SD) rats, aged 7 to 8 weeks and weighing 220–250 g, were obtained from the Laboratory Animal Center of the Air Force Military Medical University. All experimental procedures were approved by the institution's Animal Care and Use Committee. The rats were anesthetized with isoflurane, and a circular full-thickness wound (20 mm in diameter) was created on their dorsal skin. The animals were randomly divided into four groups ($n = 6$ per group): control, NPWT, control + GsMTx-4, and NPWT + GsMTx-4. NPWT was applied at −125 mmHg for 12 h per day for 7 consecutive days. To inhibit Piezo1, 300 μL of saline (vehicle) or GsMTx-4 was locally injected into the wound granulation tissue once daily at 08:00 using a 31G needle, with multipoint superficial administration at 10–12 sites around the wound edge and center(insertion depth of 1–2 mm). After a 12 h diffusion period, the animals in the NPWT groups were subjected to continuous NPWT from 20:00 to 08:00. Wound areas were photographed and measured daily from Day 0 to Day 7 to assess wound-healing dynamics. Granulation tissues were harvested on Day 4 for histological and molecular analyses.

Histology and immunohistochemistry

Granulated tissue samples were fixed in 4% PFA in PBS, followed by embedding and sectioning. The sections were deparaffinized and rehydrated before they were stained with hematoxylin and eosin (H&E) and Masson's trichrome. For immunohistochemical analysis, the following primary antibodies were used: anti-Piezo1 (Abcam, ab128245, 1:100) and anti-α-SMA (Proteintech, 14395–1-AP, 1:200). An HRP-conjugated goat anti-rabbit secondary antibody (Jackson Lab, 138729, 1:500) was used for detection. Protein expression was quantified by measuring the mean optical density using ImageJ software.

Tandem mass tag proteomics

Quantitative proteomics analysis was performed through tandem mass tag (TMT) labeling. Protein samples were prepared, trypsinized, labeled with TMT, fractionated via high-performance liquid chromatography (HPLC), and subjected to liquid chromatography–tandem mass spectrometry (LC–MS/MS) analysis. Data analysis was carried out following the procedures delineated in the Supplementary section. Hangzhou Lianchuan Biotechnology Co., Ltd, provided support for the TMT proteomics analysis.

RNA-seq (si-ctrl *vs* si-Piezo1 under negative pressure)

Total RNA extracted from rat dermal fibroblasts was isolated using TRIzol reagent (Thermo Fisher), and the quality of the RNA was assessed by a NanoDrop ND − 1000 (NanoDrop, USA). cDNA was synthesized from the fragmented RNA by using Invitrogen SuperScript™ II Reverse Transcriptase (cat. 1896649, CA, USA). RNA sequencing was conducted utilizing the Illumina NovaSeq™ 6000 platform (LC Bio Technology, China). Differential gene expression analysis was subsequently performed using the Cufflinks package and Cuffmerge (fold change > 2 and $P < 0.05$). Bioinformatic analysis was performed using the OmicStudio tools accessible at https://www.omicstudio.cn/tool; http://gepia.cancer-pku.cn/. Visual representations such as volcano plots were generated utilizing the R programming language on the OmicStudio platform (https://www.omicstudio.cn/tool).

Statistical analyses

The data are presented as the mean ± SD. The sample size (n) indicated in the figure legends corresponds to the number of independent biological replicates. The normality of the data distribution was assessed using the Shapiro–Wilk test; a P value >0.05 indicated approximate normality. For comparisons between two groups, a two-tailed Student's t test was used. For comparisons among more than two groups, one-way ANOVA was used, followed by Tukey's post hoc test. A P value <0.05 was considered to indicate statistical significance in all the experiments. All the statistical analyses were conducted using GraphPad Prism software (version 10). Statistical significance is denoted as follows: ns = not significant ($P \geq 0.05$), $^{*}P < 0.05$, $^{**}P < 0.01$, $^{***}P < 0.001$, and $^{****}P < 0.0001$.

Results

FEA of the mechanical environment in the negative pressure chamber

After the device was successfully constructed, we first verified the stability of the negative pressure output. Continuous monitoring over 24 h revealed that the device maintained a stable negative pressure with a deviation of < ±1 mmHg from the preset values, confirming the reliability of the pressure control system (Supplementary Fig. S2). We then performed a validation and analysis of the effective negative pressure space using FEA. Using the ANSYS Workbench platform, we established an accurate three-dimensional computational model of the negative pressure chamber to investigate both the velocity streamlines and the pressure distribution within the chamber environment. Our computational analysis revealed localized acceleration of flow velocities specifically concentrated at

Downloaded from academic.oup.com/burnstrauma/article/doi/10.1093/burnst/tkag007/8426274 by guest on 12 October 2026

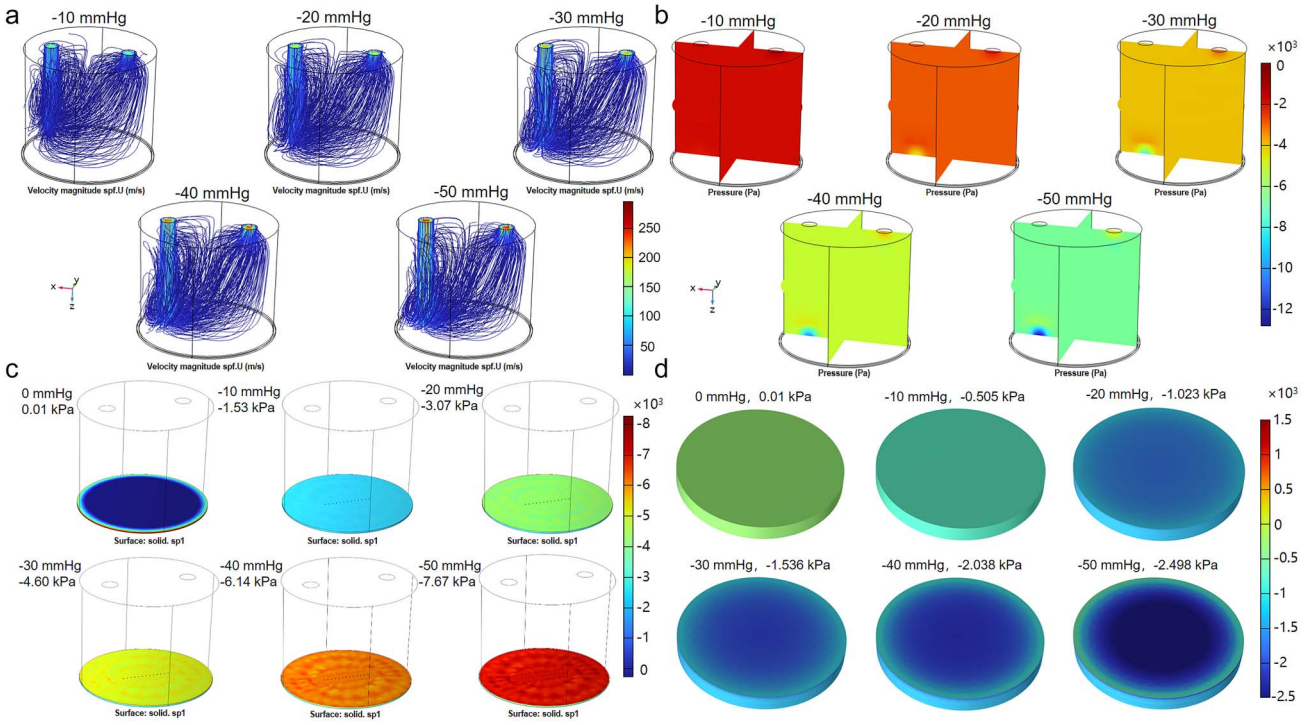


Figure 1. FEA of fluid dynamics and mechanical responses in the negative pressure loading device. (**a**) Spatial distribution of flow velocity streamlines (unit: m/s) within the gas chamber under varying negative pressures ranging from −10 to −50 mmHg. Dense streamline clusters were observed near the inlet/outlet regions. (**b**) Pressure distribution within the gas chamber under varying negative pressures. (**c**) Stress distributions (kPa) on the culture plate generated by varying negative pressures. (**d**) Cellular stress field (kPa) distribution of adherent cells subjected to varying negative pressures. Color-coded gradients depict the amplitude distributions of the velocity and pressure fields. *FEA* finite element analysis

the inlet and outlet regions. The velocity streamlines demonstrated smooth and continuous trajectories extending from the inlet to the outlet, suggesting optimal fluidic dynamics within the chamber (Fig. 1a). Furthermore, the gas chamber maintained a stable negative pressure environment characterized by a uniform pressure distribution throughout most regions, with the exception of a small area directly beneath the outlet port (Fig. 1b).

The pressure difference between the inside and outside of the chamber caused measurable deformation and displacement of the rigid culture plate. To quantify these effects, we analyzed the displacement and strain fields under various negative pressure conditions (Supplementary Fig. S3). At atmospheric pressure (0 mmHg), the culture plate showed minimal displacement and strain, mainly because of the hydrostatic pressure from the liquid medium. With increasing negative pressure, both the maximum principal strain and the maximum displacement of the culture plate displayed a linear relationship with the applied pressure (Table 1). Specifically, at −50 mmHg, the maximum displacement reached 0.77445 mm, with a maximum principal strain of 0.558%.

For cellular-level analysis, we modeled cells as circular geometries attached to the substrate, enabling us to extract the stress distribution across cell bodies. On the basis of the established pressure field and material constitutive equations, the cells experienced a hydrostatic pressure of 4.5 Pa under atmospheric conditions. We quantified the forces acting on both the culture plate and the cell bodies across a range of negative pressures (−10 to −50 mmHg; Fig. 1c and d). The results of the analysis revealed that as the negative pressure concentration increased, the compressive stress on both the culture plate and the cells increased linearly. At −50 mmHg, the compressive stress on the culture plate was −7.67 kPa, whereas the cells experienced a compressive stress of −2.486 kPa. In contrast, the tensile stress on the cells remained negligible, accounting for ∼1% of the corresponding compressive stress magnitude. These comprehensive findings provided a detailed characterization of the mechanical environment and force magnitude within the negative pressure space of our device.

NPWT treatment significantly promotes dermal fibroblast activation

Granulation tissue formation represents a critical process during the proliferative phase of wound healing, with activated dermal fibroblasts, also referred to as myofibroblasts, playing a central role [20]. These specialized cells perform essential functions in wound closure through contractile activity and extracellular matrix (ECM) production, thereby creating a structural scaffold that facilitates immune cell migration and endothelial tubulogenesis [21]. Given the pivotal role of dermal fibroblast in these biological processes, we conducted a systematic investigation into the regulatory effects of negative pressure on dermal fibroblast biological functions and phenotypic modulation using our device. In alignment with established clinical NPWT protocols that predominantly use continuous suction, we implemented a continuous NPWT regimen for our experimental design [22].

Our initial investigation focused on determining the dose-dependent effects of varying negative pressure intensities (−10 to −50 mmHg) on dermal fibroblast proliferation and differentiation (Fig. 2a–c). Negative pressure values ranging from −20 to −50 mmHg significantly increased both cellular

Downloaded from academic.oup.com/burnstrauma/article/doi/10.1093/burnst/tkag007/8426274 by guest on 12 October 2026

Table 1. Cellular deformation and characterization of stress under various negative pressure conditions

Conditions	Displacement and strain	Stress
0 mmHg	Displacement: 0.00118 mm Strain: 0.008%	Tensile stress: 0.002 kPa, Hydrostatic stress: 4.5 Pa
−10 mmHg	Displacement: 0.15489 mm Strain: 0.112%	Tensile stress: 0.008 kPa, Compressive stress: −0.505 kPa
−20 mmHg	Displacement: 0.30978 mm Strain: 0.223%	Tensile stress: 0.01 kPa, Compressive stress: −1.032 kPa
−30 mmHg	Displacement: 0.46467 mm Strain: 0.335%	Tensile stress: 0.02 kPa, Compressive stress: −1.583 kPa
−40 mmHg	Displacement: 0.61956 mm Strain: 0.447%	Tensile stress: 0.05 kPa, Compressive stress: −2.023 kPa
−50 mmHg	Displacement: 0.77445 mm Strain: 0.558%	Tensile stress: 0.08 kPa, Compressive stress: −2.468 kPa

proliferation and differentiation, with maximal stimulation observed at −40 mmHg. On the basis of these findings, we selected −40 mmHg as the optimal negative pressure intensity and determined the most effective treatment duration. CCK-8 assays and Western blot analyses revealed that 2 hours of −40 mmHg treatment elicited the most pronounced effects on dermal fibroblast activation (Fig. 2d–f). Furthermore, compared with the control group, the NPWT group exhibited markedly greater cell density, as confirmed by quantitative analysis of the live-cell images (Fig. 2g and h). Additionally, α-SMA and TGF-β1 expression was markedly upregulated in NPWT-treated dermal fibroblasts, accompanied by increased production of collagen I and Fn, indicating enhanced ECM synthesis (Fig. 2i). On the basis of these comprehensive findings, we established −40 mmHg negative pressure applied for 2 hours as the optimal treatment condition for subsequent experimental investigations.

Piezo1 may be a key regulator of the response of dermal fibroblasts to NPWT treatment

To elucidate the mechanism by which NPWT promotes dermal fibroblast activation, we performed a TMT-based quantitative proteomic analysis. Volcano plot analysis revealed 71 proteins that were differentially expressed following NPWT treatment, including 38 upregulated genes and 33 downregulated genes (Fig. 3a). GO cellular component enrichment analysis was first conducted to characterize these genes and revealed multiple enriched terms. To narrow down the targets potentially involved in mechanotransduction, a stricter enrichment threshold ($P < 0.01$) was then applied. Under these conditions, 'cortical cytoskeleton' and 'cortical actin cytoskeleton' were highlighted (Fig. S4a), from which four candidate proteins (Piezo1, Snx9, Dbn1, and Myadm) were selected for further validation. qPCR analysis revealed that Piezo1 expression most notably increased after NPWT treatment (Fig. S4b). Given its established role as a mechanosensitive cation channel in fibroblasts [23, 24], Piezo1 was chosen for further investigation. Consistent with these findings, both Piezo1 mRNA and protein levels were significantly elevated in NPWT-treated dermal fibroblasts compared with those in control dermal fibroblasts (Fig. 3b–d). Immunofluorescence staining further confirmed the substantial increase in Piezo1 expression in the NPWT group (Fig. 3e and f). To validate these findings *in vivo*, we analyzed granulation tissue from NPWT-treated rat wounds. Immunohistochemical analysis revealed marked upregulation of Piezo1 expression in the granulation tissue of the NPWT group (Fig. 3g and h). To determine whether dermal fibroblasts exhibit elevated Piezo1 expression, we performed coimmunostaining for α-SMA and Piezo1 to assess their colocalization in granulation tissue. Immunofluorescence analysis revealed a strong correlation between Piezo1 expression and α-SMA levels in granulation tissue (Fig. 3i–l). Taken together, these findings suggest that Piezo1 may play a critical role in the mechanotransductive activation of dermal fibroblast under NPWT treatment.

Piezo1 mediates NPWT-induced granulation tissue formation *in vivo*

To determine whether Piezo1 is responsible for the ability of NPWT to promote granulation tissue formation, we established full-thickness skin defects in rats and subjected them to one of four treatments: (i) administration of the Piezo1 inhibitor GsMTx-4 (300 μL, 5 μM) [25], (ii) NPWT alone, (iii) NPWT combined with GsMTx-4, or (iv) no treatment (control). Macroscopic images of wound granulation tissue revealed that compared with the control treatment, NPWT significantly enhanced granulation tissue formation. However, these effects were attenuated by coadministration of GsMTx-4 (Fig. 4a). Microscopic examination further demonstrated that GsMTx-4 the expression of the proliferation marker PCNA (Fig. 4b–g). Consistently, daily measurements of the wound area from Day 0 to Day 7 revealed that compared with the control treatment, NPWT accelerated wound closure, whereas GsMTx-4 treatment attenuated this effect (Supplementary Fig. S5). To investigate the role of Piezo1 in dermal fibroblast activation, we extracted total protein from granulation tissue and analyzed the expression of dermal fibroblast activation markers. Western blot analysis confirmed that GsMTx-4 markedly inhibited the NPWT-induced upregulation of α-SMA, TGF-β1, collagen I, and Fn expression (Fig. 4h–l). Collectively, these results suggest that Piezo1 activity plays a critical role in mediating NPWT-driven fibroblast activation and granulation tissue formation.

Piezo1 mediates NPWT-induced dermal fibroblast activation *in vitro*

Building on the *in vivo* findings, we next investigated the role of Piezo1 in NPWT-induced dermal fibroblast activation. To this end, we used two complementary strategies: pharmacological inhibition with the Piezo1 antagonist GsMTx-4 and siRNA-mediated knockdown of Piezo1. The efficiency of

Downloaded from academic.oup.com/burnstrauma/article/doi/10.1093/burnst/tkag007/8426274 by guest on 12 October 2026

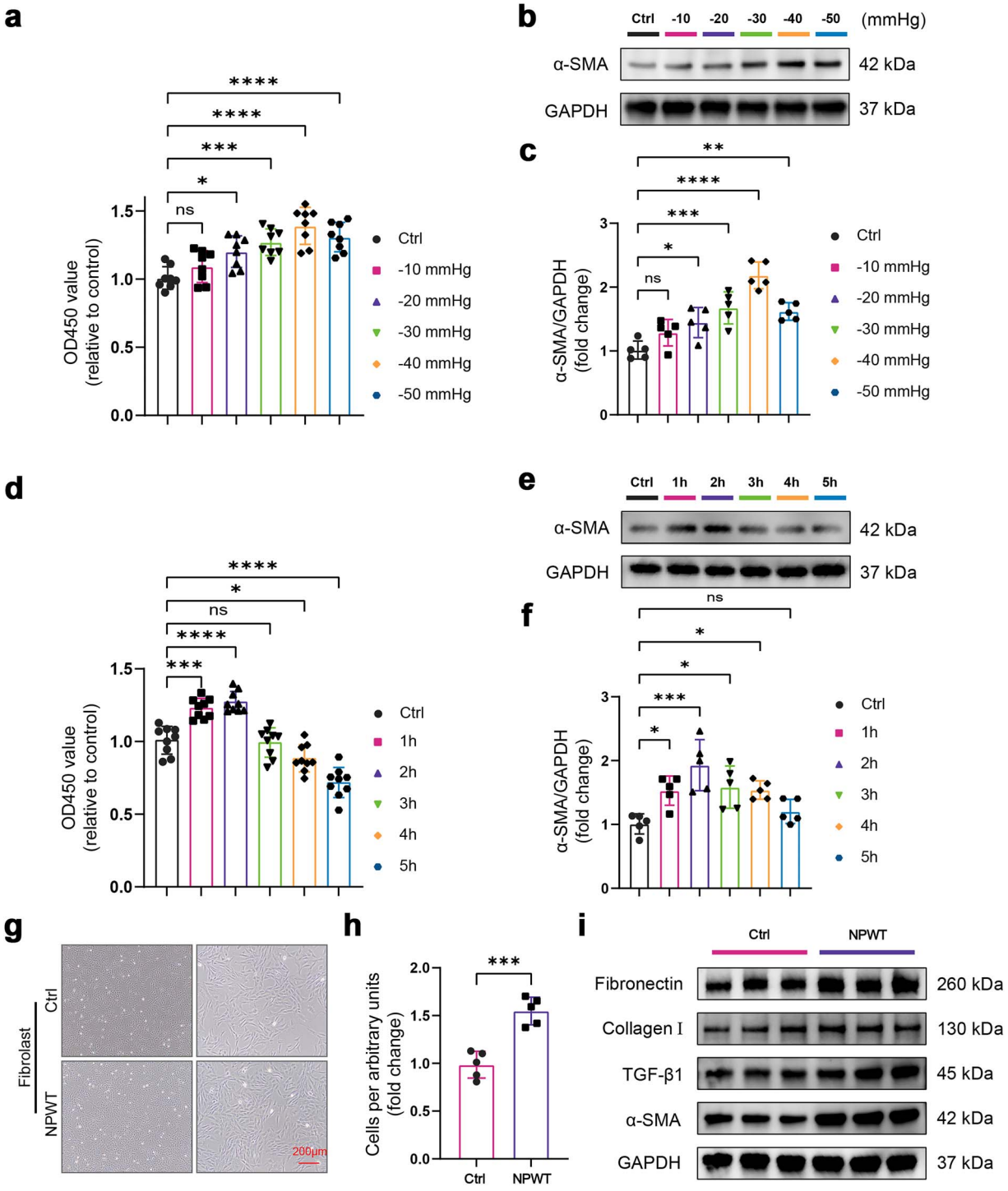


Figure 2. NPWT treatment promotes dermal fibroblast proliferation and differentiation. (**a**) The cell proliferation rate was measured by a CCK-8 assay in a strength-dependent manner. n = 8 per group. (**b**, **c**) Western blotting analysis of α-SMA in dermal fibroblasts subjected to different negative pressures. n = 5 per group. (**d**) The cell proliferation rate was measured by a CCK-8 assay in a time-dependent manner. n = 8 per group. (**e**, **f**) Western blotting analysis of α-SMA in dermal fibroblasts subjected to −40 mmHg negative pressures for varying durations (0–5 h). n = 5 per group. (**g**) Representative live-cell images of the NPWT-treated and control groups (scale bar: 200 μm). (**h**) Quantification of cell density based on live-cell imaging. n = 5 per group. (**i**) The effects of negative pressure on the expression of fibronectin, collagen I, TGF-β1, and α-SMA were assessed by western blotting. *ns* not significant, * $P < 0.05$, ** $P < 0.01$, *** $P < 0.001$, and **** $P < 0.0001$. *NPWT* negative pressure wound therapy, *DF* dermal fibroblast, *α-SMA* α-smooth muscle actin, *TGF-β1* transforming growth factor beta1, *CCK-8* cell counting kit-8

Piezo1 knockdown was confirmed by assessing both mRNA and protein expression levels (Supplementary Fig. S6). We first evaluated dermal fibroblast proliferative capacity using Ki67 immunofluorescence staining. NPWT treatment significantly increased the percentage of Ki67-positive cells compared with that in the static control group. In contrast, both GsMTx-4 treatment and Piezo1 knockdown markedly suppressed NPWT-induced dermal fibroblast proliferation (Fig. 5a–d). To

Downloaded from academic.oup.com/burnstrauma/article/doi/10.1093/burnst/tkag007/8426274 by guest on 12 October 2026

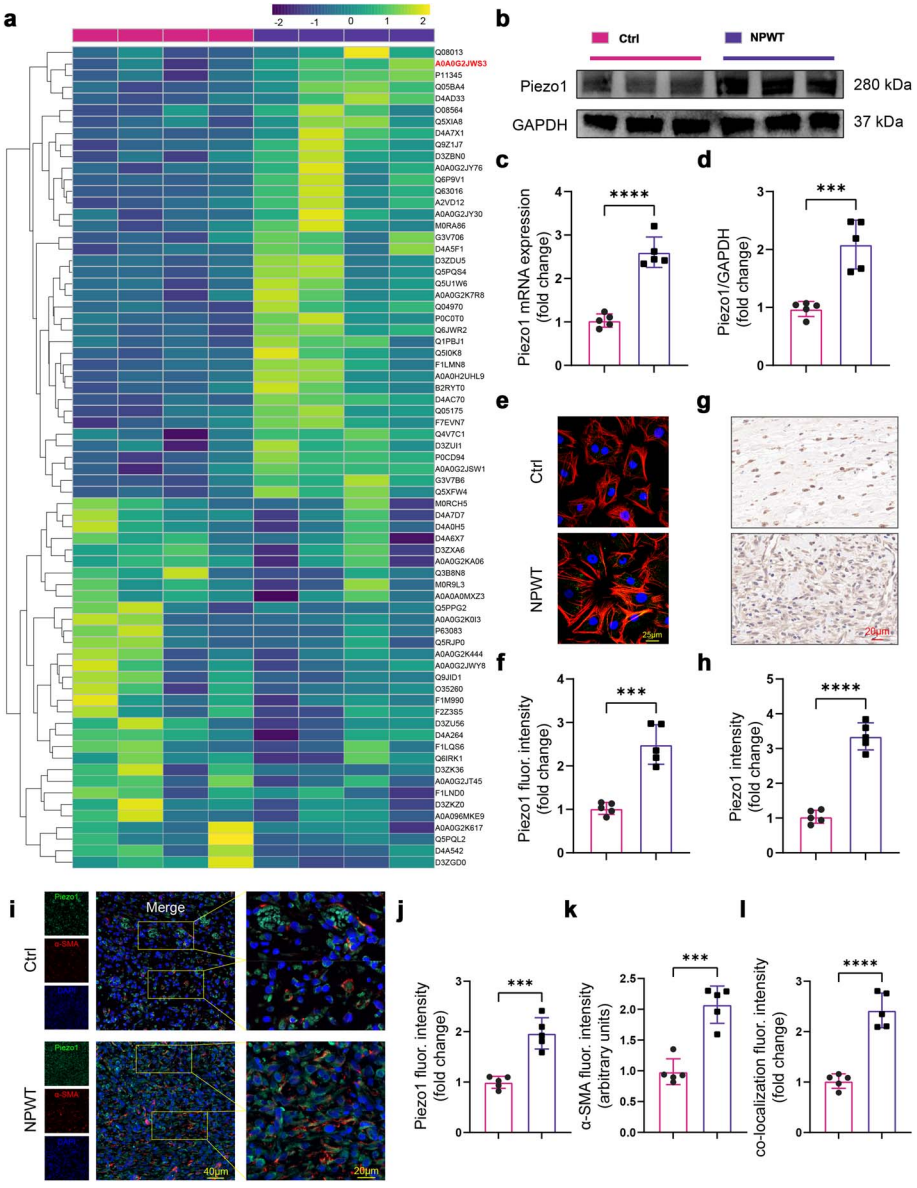


Figure 3. NPWT treatment can induce significant upregulation of Piezo1 in dermal fibroblasts. (**a**) Differentially expressed gene profiling based on TMT proteomics (NPWT *vs* control). n = 4 per group. (**b–d**) The effects of NPWT treatment on the expression of Piezo1 in dermal fibroblasts were assessed by RT–qPCR and western blotting. n = 5 per group. (**e**, **f**) Immunofluorescence staining analysis of Piezo1 in dermal fibroblasts subjected to NPWT (scale bar: 25 μm). n = 5 per group. (**g**, **h**) Images and quantitative analysis of immunohistochemical staining for Piezo1 in rat granulation tissue (scale bar: 20 μm). n = 5 per group. (**i**) Representative immunofluorescence images showing coimmunostaining of Piezo1 and α-SMA in granulation tissue. Piezo1 is labeled in green, and α-SMA is in red (scale bar: 40 μm). (**j–l**) Quantification of Piezo1 expression, α-SMA expression, and their colocalization using Mander's overlap coefficient. n = 5 per group. $^{*}P < 0.05$, $^{**}P < 0.01$, $^{***}P < 0.001$, and $^{****}P < 0.0001$. *NPWT* negative pressure wound therapy, *DF* dermal fibroblast, *α-SMA* α-smooth muscle actin, *TMT* tandem mass tag

further assess dermal fibroblast activation and ECM secretion, we analyzed protein extracts from the four experimental groups via Western blotting (Fig. 5e-i). The results demonstrated elevated expression levels of α-SMA and TGF-β1 in the NPWT-treated group. Notably, GsMTx-4 treatment attenuated the overexpression of α-SMA in fibroblasts cultured under NPWT conditions. Additionally, collagen I and Fn expression was upregulated in fibroblasts following NPWT treatment, whereas inhibition of Piezo1 function significantly impaired ECM secretion by dermal fibroblasts. Immunofluorescence staining of α-SMA further corroborated these findings, which aligned with the Western blotting results (Fig. 5j–k). To further validate the specificity of Piezo1 in this process, we performed an additional control experiment using a selective TRPV4 inhibitor (GSK2193874, 3 nM), as TRPV4 is another mechanosensitive Ca^{2+} channel expressed in dermal fibroblasts [26]. NPWT-induced upregulation of dermal fibroblast activation markers remained largely unaffected by TRPV4 inhibition, whereas Piezo1 blockade markedly attenuated these effects (Supplementary Fig. S7), supporting the predominant role of Piezo1 in NPWT-triggered mechanotransduction. Taken together, these findings indicate that NPWT promotes dermal fibroblast activation through a mechanism mediated by Piezo1.

Downloaded from academic.oup.com/burnstrauma/article/doi/10.1093/burnst/tkag007/8426274 by guest on 12 October 2026

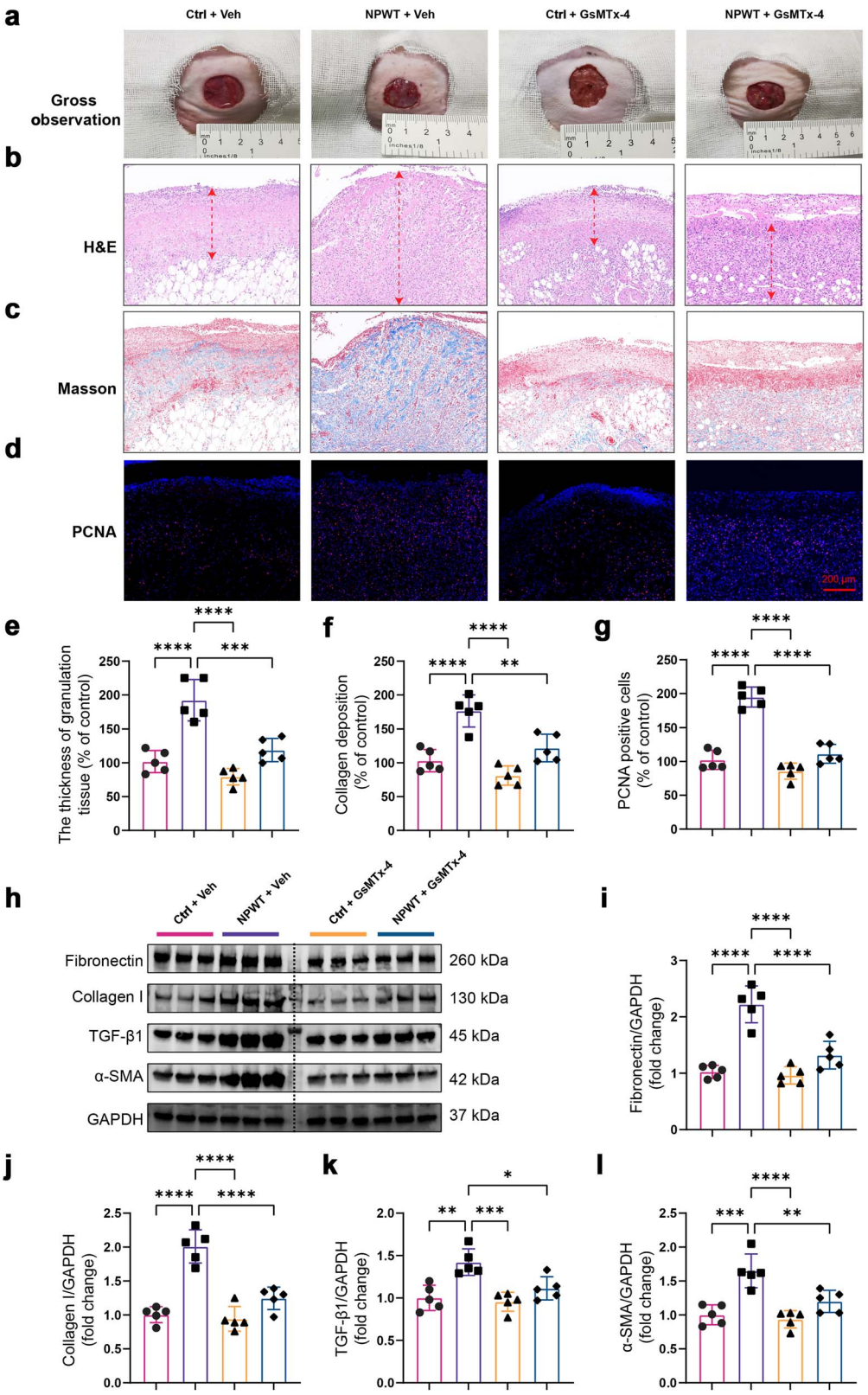


Figure 4. Piezo1 inhibition attenuates NPWT-driven granulation formation. (**a**) Representative macroscopic images of wound granulation tissues on Day 4 across the experimental groups: Ctrl +Veh, NPWT + Veh, Ctrl + GsMTx-4, NPWT + GsMTx-4. (**b**, **c**) Representative images of granulation tissues stained by HE and Masson's trichrome. In panel b, dashed arrows indicate the measurement boundaries used for granulation tissue thickness assessment (scale bar: 200 μm). (**d**) Immunofluorescence staining of PCNA in granulation tissue (PCNA and DAPI channels shown; scale bar: 200 μm). (**e**–**g**) Quantitative analysis of the thickness of granulation tissue, collagen deposition, and PCNA-positive cells. (**h**–**l**) Representative western blotting images and quantitative analysis of the expression of fibronectin, collagen I, TGF-β1, and α-SMA in each group. n=5 per group. $^{*}P$ <0.05, $^{**}P$ <0.01, $^{***}P$ <0.001, and $^{****}P$ <0.0001. *NPWT* negative pressure wound therapy, *PCNA* proliferating cell nuclear antigen, *α-SMA* α-smooth muscle actin, *TGF-β1* transforming growth factor beta1

Downloaded from academic.oup.com/burnstrauma/article/doi/10.1093/burnst/tkag007/8426274 by guest on 12 October 2026

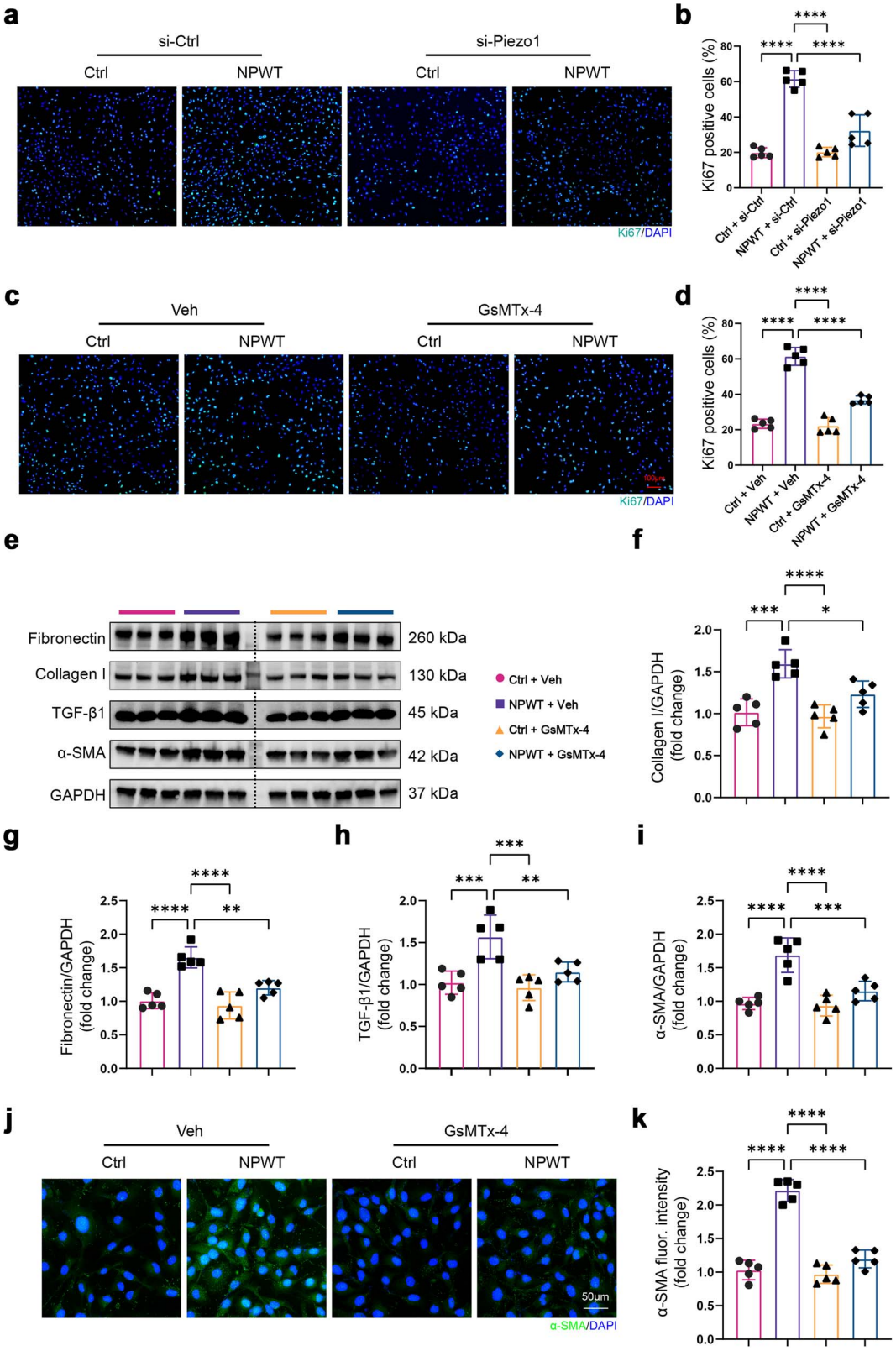


Figure 5. Piezo1 inhibition attenuates NPWT-induced dermal fibroblast activation. (**a**) Representative immunofluorescence images showing Ki67-positive dermal fibroblasts treated with Piezo1 knockdown (Scale bar: 100 μm). (**b**) Quantitative analysis of the percentage of Ki67-positive cells. (**c**) Representative immunofluorescence images showing Ki67-positive dermal fibroblasts with GsMTx-4 (Scale bar: 100 μm). (**d**) Quantitative analysis of the percentage of Ki67-positive cells. (**e**–**i**) Representative western blotting images and quantitative analysis of the expression of fibronectin, collagen I, TGF-β1, and α-SMA in the 4 groups: Ctrl + Veh, Ctrl + GsMTx-4, NPWT + Veh, and NPWT + GsMTx-4. (**j**, **k**) Immunofluorescence analysis of α-SMA in dermal fibroblasts subjected (or not subjected) to NPWT treatment and treated (or not treated) with GsMTx-4 (scale bar: 50 μm). n = 5 per group. $^{*}P < 0.05$, $^{**}P < 0.01$, $^{***}P < 0.001$, and $^{****}P < 0.0001$. *NPWT* negative pressure wound therapy, *DF* dermal fibroblast, *α-SMA* α-smooth muscle actin, *TGF-β1* transforming growth factor beta1, *Veh* vehicle

Downloaded from academic.oup.com/burnstrauma/article/doi/10.1093/burnst/tkag007/8426274 by guest on 12 October 2026

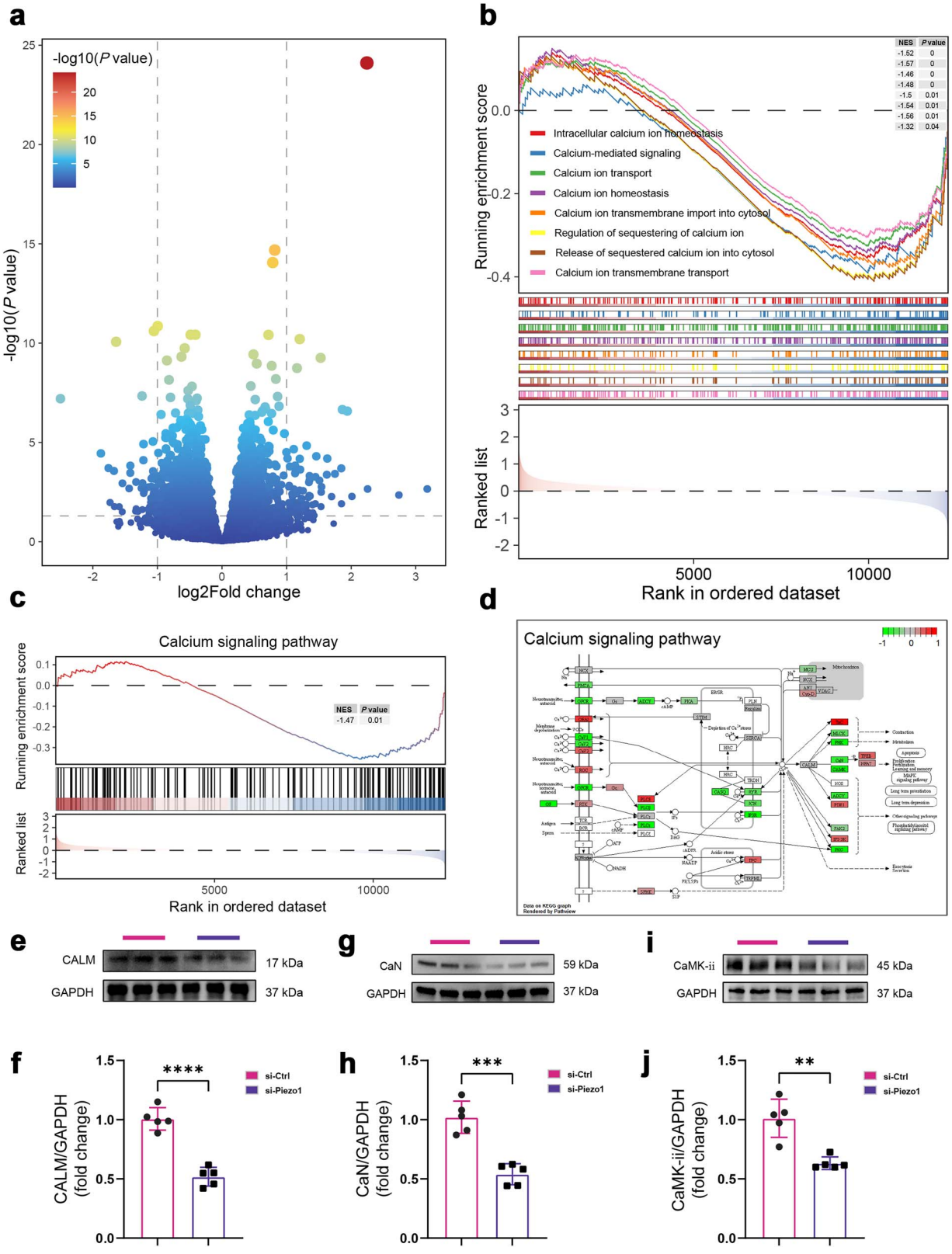


Figure 6. NPWT treatment promotes dermal fibroblast activation via the Piezo1-mediated calcium signaling pathway. (**a**) Volcano plot of differentially expressed genes (DEGs) in Piezo1 knockdown (si-Piezo1) versus control (si-Ctrl) dermal fibroblasts treated with NPWT. (**b**, **c**) GSEA revealed significant suppression of calcium-related signaling pathways upon Piezo1 knockdown. (**d**) Network of DEGs associated with the CaN/NFAT signaling axis. (**e–j**) Western blotting analysis of the expression of CALM, CaN, and CaMK-ii in dermal fibroblasts with NPWT treatment. Representative images of three independent experiments are shown. n = 5 per group. *ns* not significant, $^{*}P < 0.05$, $^{**}P < 0.01$, $^{***}P < 0.001$, and $^{****}P < 0.0001$. *NPWT* negative pressure wound therapy, *DF* dermal fibroblast, *DEG* differentially expressed gene, *CALM* calmodulin, *CaN* calcineurin, *CaMK-ii* calmodulin-dependent protein kinase ii

Downloaded from academic.oup.com/burnstrauma/article/doi/10.1093/burnst/tkag007/8426274 by guest on 12 October 2026

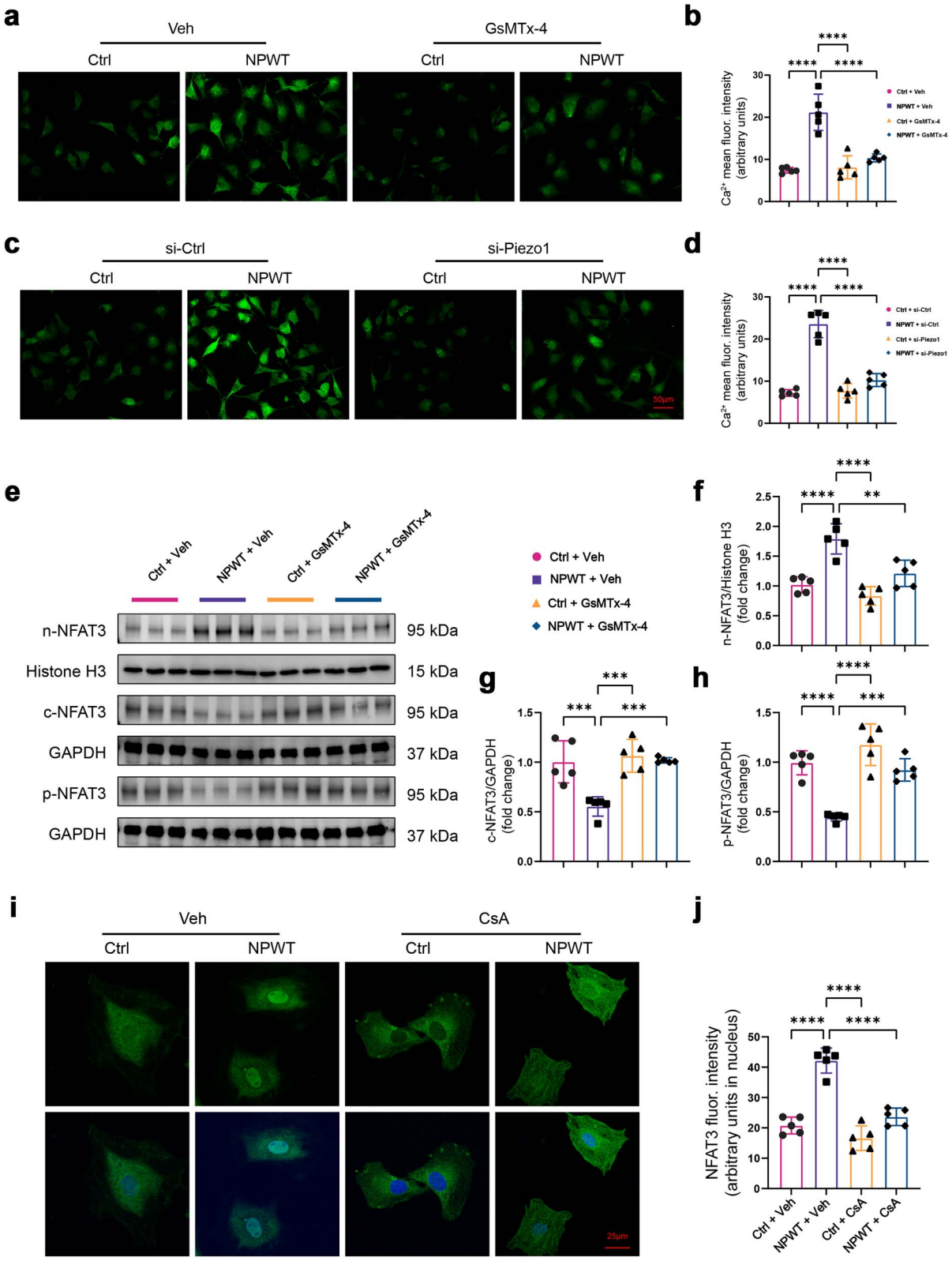


Figure 7. NPWT activates dermal fibroblasts via the Piezo1-Ca^{2+}-CaN/NFAT3 signaling axis. (**a**) Representative immunofluorescence images of intracellular Ca^{2+} in dermal fibroblasts treated with GsMTx-4 (scale bar: 50 μm). (**b**) Quantification of the mean fluorescence intensity of Ca^{2+} in dermal fibroblasts. (**c**) Representative immunofluorescence images of intracellular Ca^{2+} in dermal fibroblasts with Piezo1 knockdown (scale bar: 50 μm). (**d**) Quantification of the mean fluorescence intensity of Ca^{2+} in dermal fibroblasts. (**e**–**h**) Western blotting was performed to analyze nuclear NFAT3 (n-NFAT3), cytoplasmic NFAT3 (c-NFAT3), and phosphorylated NFAT3 (p-NFAT3) in dermal fibroblasts from the four experimental groups. GAPDH and Histone H3 were used as cytoplasmic and nuclear loading controls, respectively. (**i**, **j**) Immunofluorescence staining analysis of NFAT3 in CsA-treated dermal fibroblasts under NPWT treatment. (scale bar: 25 μm). n = 5 per group. *ns* not significant, $^{*}P < 0.05$, $^{**}P < 0.01$, $^{***}P < 0.001$, and $^{****}P < 0.0001$. *NPWT* negative pressure wound therapy, *DF* dermal fibroblast, *NFAT3* nuclear factor of activated T cells 3, *CsA* cyclosporin A

Downloaded from academic.oup.com/burnstrauma/article/doi/10.1093/burnst/tkag007/8426274 by guest on 12 October 2026

Piezo1 coordinates calcium signaling to drive NPWT-induced dermal fibroblast activation

Given the pivotal role of Piezo1 in mediating NPWT-induced dermal fibroblast activation, we investigated the downstream mechanotransduction pathways involved. RNA-seq was performed on NPWT-treated dermal fibroblasts following siRNA-mediated Piezo1 knockdown (si-Piezo1) or control transfection (si-Ctrl). Differential gene expression analysis (fold change >2, $P < 0.05$), as visualized by volcano plots, revealed a total of 353 significantly downregulated and 269 significantly upregulated mRNAs in si-Piezo1-treated cells (Fig. 6a). Gene-set enrichment analysis (GSEA) across the Gene Ontology (GO) biological process, cellular component, and molecular function categories revealed pronounced enrichment of calcium-related signaling pathways. Consistently, Kyoto Encyclopedia of Genes and Genomes pathway analysis revealed marked suppression of calcium signaling in the si-Piezo1 group (Fig. 6b and c).

Because Piezo1 functions as a mechanosensitive ion channel, we hypothesized that the decrease in dermal fibroblast activation upon Piezo1 knockdown under NPWT is primarily due to the disruption of downstream Ca^{2+} signaling. To further elucidate the underlying regulatory mechanisms, we conducted network analysis of the RNA-seq data, aiming to pinpoint key pathways and genes implicated in the observed transcriptional signature (Fig. 6d). Within this network, we detected significant downregulation of calcineurin (CaN) and calcium/calmodulin (CALM)-dependent protein kinase (CAMK), which are well known to regulate cellular proliferation, differentiation, and related phenotypes [27]. To validate these findings, we assessed the protein expression levels of three core components by Western blotting. Compared with the control group, the si-Piezo1 group exhibited markedly reduced expression levels of CALM, CaN, and CaMK-ii (Fig. 6e–j). Collectively, these data demonstrate that Piezo1 promotes NPWT-induced dermal fibroblast activation through calcium-dependent signaling pathways.

NPWT induces Piezo1-dependent calcium influx to potentiate the CaN/NFAT3 signaling axis in dermal fibroblasts

To determine whether Piezo1 serves as the principal mediator of NPWT-induced calcium influx in dermal fibroblasts, we performed intracellular Ca^{2+} imaging using the fluorescent indicator Fluo 3-AM. NPWT treatment triggered a robust increase in intracellular Ca^{2+} levels. Notably, both pharmacological and genetic inhibition of Piezo1 expression abolished NPWT-driven calcium influx, indicating that Piezo1 is the key mechanosensitive channel that mediates calcium influx under NPWT (Fig. 7a–d). To further characterize the temporal dynamics of this process, time-lapse Ca^{2+} imaging was conducted during NPWT exposure. The fluorescence signals were recorded at baseline (0 h), 1 h, and 2 h following −40 mmHg stimulation. Consistent with the results of the endpoint analysis, intracellular Ca^{2+} levels progressively increased over time in the si-Ctrl + NPWT group, whereas this time-dependent increase was substantially blunted upon Piezo1 knockdown (Supplementary Fig. S8), confirming that NPWT-evoked Ca^{2+} influx is both dynamic and Piezo1 dependent.

Building on the differentially expressed gene network analyses described above, we focused on the CaN/NFAT signaling axis. Prior studies have established that elevated cytosolic Ca^{2+} levels cooperate with calmodulin to activate CaN, which in turn dephosphorylates nuclear factor of activated T cells (NFAT), enabling its nuclear translocation and regulation of proliferation/differentiation [27]. To evaluate the involvement of this pathway, we examined the nuclear distribution of NFAT1–4 by Western blotting and found that NPWT treatment markedly increased the nuclear accumulation of NFAT3 (Supplementary Fig. S9). To confirm the influence of Piezo1 on NFAT3 activation, we performed Western blot analysis under various intervention conditions (Fig. 7e–h). Our results demonstrated that NPWT treatment increased NFAT3 nuclear localization while simultaneously reducing its cytoplasmic levels and overall phosphorylation. In contrast, Piezo1 inhibition impaired NPWT-induced NFAT3 nuclear translocation and increased its phosphorylation level.

Moreover, to further validate the contribution of CaN to NPWT-induced NFAT activation, we treated NPWT-exposed DFs with cyclosporine A (CsA), a selective calcineurin inhibitor [28]. Immunofluorescence staining revealed that NPWT treatment promoted NFAT3 nuclear accumulation, whereas CsA administration effectively prevented this translocation (Fig. 7i; representative multicellular immunofluorescence images illustrating NFAT3 nuclear localization have been included in the Supplementary Fig. S10a for further visualization). Quantitative analysis further corroborated this effect at the multicellular level (Fig. 7j). To further confirm the causal role of Ca^{2+} influx in downstream NFAT3 activation, we performed additional experiments using the Ca^{2+} chelator BAPTA-AM. Western blot analysis revealed that NPWT significantly promoted NFAT3 nuclear translocation, whereas BAPTA-AM pretreatment effectively abolished this effect (Supplementary Fig. S10b–c). Finally, we evaluated the functional consequences of CaN inhibition on NPWT-induced dermal fibroblast activation. CsA treatment attenuated the expression of α-SMA, TGF-β1, collagen I, and PCNA, indicating a marked reduction in DF activation under NPWT conditions (Supplementary Fig. S11). Together, these findings demonstrate that NPWT treatment enhances NFAT3 dephosphorylation and nuclear localization through Piezo1-mediated Ca^{2+} influx, ultimately activating downstream pathways involved in dermal fibroblast activation.

To further elucidate the transcriptional landscape associated with NFAT3 activity, we integrated the Gene Expression Profiling Interactive Analysis (GEPIA) and human skin RNA-seq datasets to explore its potential regulatory network. NFATc4 (NFAT3) expression strongly positively correlated with the expression of fibroblast activation–related genes, including ACTA2 (α-SMA, $R = 0.40$, $P = 2.3 \times 10^{-10}$), COL1A1 (Collagen I, $R = 0.38$, $P = 1.5 \times 10^{-9}$), TGFB1 (TGF-β1, $R = 0.28$, $P = 9.9 \times 10^{-6}$), and FN1 (Fibronectin, $R = 0.51$, $P \approx 0$). These transcriptomic associations highlight a potential NFAT3-centred profibrotic transcriptional module that may underlie NPWT-induced dermal fibroblast activation (Supplementary Fig. S12).

Discussion

NPWT is a mechanical stimulation method that greatly enhances granulation tissue formation in wounds. However, the mechanisms of mechanotransduction involved in this therapy are still unclear, mainly because of the absence of accurate and controlled negative pressure devices for *in vitro* use. In

Downloaded from academic.oup.com/burnstrauma/article/doi/10.1093/burnst/tkag007/8426274 by guest on 12 October 2026

this study, we developed a high-performance *in vitro* negative pressure loading cultivation system compatible with six-well plates. This system enables independent and intelligent adjustment of negative pressure levels, durations, and modes for each well, making it the most comprehensive *in vitro* negative pressure device currently available. Additionally, we validated its effectiveness through FEA, elucidating the magnitude and nature of cellular forces. Using this device, we further discovered that a continuous negative pressure of −40 mmHg (∼2 kPa) applied for two hours significantly activated dermal fibroblasts by enhancing the activity of the Piezo1/calcineurin/NFAT3 signaling pathway.

Owing to the lack of *in vitro* negative pressure devices, research on negative pressure biomechanics has lagged behind clinical studies and applications. Since 2007, only two *in vitro* negative pressure models have been reported. The earliest model utilized a perfusion bioreactor, where a fibrin matrix was used to construct a three-dimensional cell culture scaffold integrated into the bioreactor module. After polyurethane foam was placed on top of the culture matrix, the device was sealed, and negative pressure was applied, causing the culture medium to circulate under negative pressure [16]. However, this setup requires stringent laboratory conditions and faces reproducibility challenges. Additionally, the mechanical environment exerted on cells is complex and involves fluid shear stress, tensile forces, and negative pressure, making isolation of the effects of individual mechanical stimuli on cellular phenotypes difficult. Consequently, this model has not gained widespread adoption. Alternatively, simpler setups created negative pressure environments for two-dimensional cell cultures. For example, Shou et al. [5] inserted a needle connected to an negative pressure pump directly into a culture flask to apply −150 mmHg negative pressure; Pandit et al. [6] placed six-well plates inside sealed bags and applied 15 kPa (≈ −110 mmHg) negative pressure; Khalifa et al. [7] used transparent acrylic negative pressure chambers to apply −50 mmHg negative pressure, inducing hepatocyte dedifferentiation. These devices, while easy to construct, typically feature only exhaust ports without air inlets, potentially disrupting necessary gas exchange for normal cell culture. Zhang et al. improved upon this by designing a larger sealed glass chamber with both exhaust and inlet ports connected to an negative pressure pump, facilitating gas exchange [29]. Hsu et al. further optimized the in vitro negative pressure environment by developing negative pressure incubators that simulate cellular culture conditions, including temperature, humidity, and CO_2/O_2 levels [30]. Although these advancements ensured proper culture conditions, the larger negative pressure spaces remained cumbersome to operate and lacked precise negative pressure control. Moreover, none of the reported devices validated the effectiveness of the negative pressure environment. To address these limitations, we selected six-well plates to explore negative pressure gradients and designed a single-well negative pressure space with a height of 3 cm and a diameter of 3.5 cm, which was significantly smaller than previously reported custom chambers. Our device achieves negative pressure precision within ±1 mmHg. The negative pressure regulatory components are housed within the incubator, maintaining a conducive environment for cell growth. An external integrated electrical control system allows independent adjustment of the negative pressure levels and modes for each well. FEA revealed that our device maintained a uniform and stable negative pressure environment, with the compressive stress on the culture plates and cells increasing linearly with negative pressure. In summary, our device offers high precision, automation, and ease of use without compromising cell viability, providing a robust platform for advancing negative pressure biomechanics research.

Using our *in vitro* negative pressure device, we conducted preliminary investigations into the effects of negative pressure biomechanics on dermal fibroblasts. We observed that applying −40 mmHg negative pressures for two hours significantly activated the dermal fibroblasts. These parameters are milder than those in most existing studies, which report optimal negative pressure ranging from −50 to −200 mmHg and durations between one and 48 hours. For example, Hsu et al. [30] utilized a custom negative pressure cell culture chamber with negative pressure concentrations of −75, −125, and − 175 mmHg for 6 and 12 hours and reported that −125 mmHg for 12 hours notably promoted keratinocyte migration. Similarly, Zhang et al. [29] used a cubic negative pressure chamber with gradients of −75, −125, −200, and − 250 mmHg for 48 hours and demonstrated that −200 mmHg significantly enhanced osteoblast differentiation. Jin et al. [14] applied negative pressure levels of ∼−380, −152, −75, −50, and − 38 mmHg for 4 hours and reported that −50 and − 38 mmHg promoted dermal fibroblast proliferation without inducing significant migration, with −38 mmHg showing a more pronounced effect (see Supplementary materials). Our findings partially align with these studies; however, the longer negative pressure durations in previous research may reflect higher tolerance in human cell lines. Overall, *in vitro* negative pressure biomechanics research remains limited, particularly in terms of optimizing negative pressure conditions. Existing devices are generally simple and self-constructed and often feature large negative pressure spaces that may compromise negative pressure accuracy and stability. In contrast, our device uses a compact negative pressure space (3.5 cm diameter, 3 cm height) with precise NP control (±1 mmHg) and real-time monitoring through integrated sensors. These advancements likely account for the discrepancies between our data and those of prior reports. Additionally, variations in NP requirements across different cell species, types, and phenotypes highlight the need for further investigations in future studies.

Notably, the negative pressure parameters used in our *in vitro* model differ from those commonly applied in clinical NPWT. This divergence is largely attributable to differences in biological context and therapeutic objectives. Clinical NPWT typically involves the application of high pressures (−75 to −125 mmHg) to achieve multiple synergistic effects—such as wound contraction, exudate removal, edema reduction, and microenvironment stabilization [1]. In contrast, our *in vitro* system was intentionally designed as a reductionist model to isolate mechanical stimulation as a single variable and evaluate its direct mechanotransductive impact of negative pressure on cells. Moreover, the effective pressure acting on wound tissues *in vivo* is substantially attenuated by dressing materials and the intrinsic buffering capacity of three-dimensional tissue architecture, indicating that cells rarely experience full applied pressure [31, 32]. Indeed, for fragile or ischemic wounds, clinical guidelines often recommend milder pressures (−60 to −80 mmHg), which approximate the optimal range identified in our study [22]. These distinctions underscore that our model is not intended to replicate clinical NPWT in its entirety but rather to mechanistically elucidate the cellular response to

Downloaded from academic.oup.com/burnstrauma/article/doi/10.1093/burnst/tkag007/8426274 by guest on 12 October 2026

negative pressure—providing a foundational framework that complements rather than replaces clinical investigations.

Moreover, we used TMT proteomics to identify key protein molecules involved in cellular responses to NPWT. Among these differentially expressed proteins, Piezo1 was notably upregulated. Piezo1 is a recently identified mechanosensitive ion channel that detects mechanical stimuli and mediates calcium ion influx [33]. Studies have demonstrated that Piezo1 plays a crucial role in the mechanotransduction responses of various skin cell types [34–36]. Additionally, He et al. [25] reported that enhancing Piezo1 activity promotes dermal fibroblast proliferation, migration, and differentiation. Jin et al. [14] reported that NPWT therapy increases intracellular calcium concentrations and promotes keratinocyte migration; however, these effects were significantly diminished or abolished when calcium channel blockers were used. Despite these insights, the specific calcium channels involved remain unclear. Building on the findings of Jin et al., we propose that Piezo1 is a critical protein that mediates dermal fibroblast responses to the NPWT. Activation of Piezo1 facilitates increased calcium influx, triggering downstream signaling cascades. Both *in vitro* and *in vivo* experiments confirmed that NPWT treatment increased Piezo1 expression and activity. Furthermore, disrupting Piezo1 function or expression significantly reduced dermal fibroblast activation levels. Our study is the first to elucidate the pivotal role of Piezo1 in the mechanotransduction process underlying dermal fibroblast activation in response to NPWT treatment.

Although Piezo1 is a mechanosensitive ion channel whose primary function involves Ca^{2+} signaling upon activation, several studies have reported its interactions with other signaling pathways. For instance, in glioma, Piezo1 regulates integrin-FAK signaling to promote cancer cell survival and invasion [37]. In adipose tissue, Piezo1 enhances adipogenesis through the FGF1/FGFR1 pathway [38]. In bone, Piezo1 activates β-catenin and its target gene ATF4, thereby promoting the proliferation and osteogenic differentiation of bone marrow mesenchymal stem cells [39]. These findings indicate that Piezo1-mediated downstream signaling pathways have diverse functions across different cell types and pathological processes. To further elucidate the mechanotransduction process mediated by Piezo1 under NPWT conditions, we performed high-throughput RNA-seq on two groups of dermal fibroblasts treated with either si-Ctrl or si-Piezo1 under identical NPWT conditions. GO and GSEA revealed that alterations in calcium signaling pathways were the most significant. On the basis of the RNA-seq data, we identified pathways and genes closely associated with specific gene signatures and conducted network analysis to identify genes that are differentially expressed downstream of the calcium influx signaling pathway. The results revealed that these genes were significantly enriched in the calcineurin/NFAT3 pathway. Subsequent experiments demonstrated that NPWT treatment induced Piezo1-dependent Ca^{2+} influx, which activated calcineurin, leading to the nuclear translocation of NFAT3 and subsequent activation of dermal fibroblasts.

Despite these promising findings, several limitations should be acknowledged. First, in our FEA model, dermal fibroblasts were simplified as circular geometries to enhance computational efficiency and analytical clarity. This geometric approximation does not fully capture the elongated morphology and heterogeneous cytoskeletal architecture of native dermal fibroblasts, which may affect their local mechanical responses and stress distributions under NPWT stimulation. Second, although the model provides valuable insights into the spatial pressure field, direct experimental validation of the FEA predictions is still lacking. We are currently working on integrating high-resolution laser displacement sensors into the device to facilitate quantitative validation in future iterations. Third, the upstream regulatory mechanism of NPWT-induced Piezo1 upregulation was not examined in this study, and its regulatory basis warrants further investigation.

Calcium influx signaling and the calcineurin-NFAT pathway are critical for dermal fibroblast activation during normal wound healing. Davis et al. reported that the TRPC6-mediated NFAT pathway is essential for myofibroblast differentiation and that TRPC6 deficiency delays wound healing, a phenotype that can be rescued by sustained calcineurin activity [40]. Additionally, CsA injections significantly reduce wound contraction and the expression of hydroxyproline accumulation-related markers of reparative collagen deposition, highlighting the role of the NFAT pathway in promoting granulation tissue formation [28]. Notably, microamperage electrical stimulation has been shown to enhance NFAT activation, thereby promoting dermal collagen synthesis, accelerating granulation and re-epithelialization, and improving wound healing efficacy [41]. Furthermore, electrical stimulation facilitates cardiac fibroblast proliferation through NFAT activation [42]. Our study demonstrated that NPWT enhances the calcineurin/NFAT3 pathway, thereby promoting DF activation.

Conclusions

In this study, we successfully developed a high-performance *in vitro* negative pressure loading cultivation device compatible with six-well plates, enabling independent and intelligent control of negative pressure levels, durations, and modes for each well. This device addresses a critical gap in negative pressure biomechanics research by providing a controllable and precise platform for cellular negative pressure stimulation. We validated its efficacy by establishing a three-dimensional physical model of a single-well negative pressure space and conducting FEA, which elucidated the magnitude and nature of cellular forces under negative pressure conditions. Our findings demonstrated that applying −40 mmHg negative pressures for 2 hours significantly activates dermal fibroblast. Furthermore, for the first time, we elucidated the molecular mechanism by which NPWT promotes dermal fibroblast activation through the Piezo1-mediated calcineurin/NFAT3 signaling pathway. This study lays a foundational framework for further negative pressure biomechanics research and offers new avenues for tissue engineering and regenerative medicine.

Ethical approval

All experimental protocols were performed in accordance with the Guide for Using Animal Subjects and were subject to approval by the experimental animal center of the Xijing Hospital of Fourth Military Medical University (No. 20240251).

Supplementary material

Supplementary material is available at *Burns & Trauma Journal* online.

Conflicts of interest

The authors declare that they have no competing interests.

Downloaded from academic.oup.com/burnstrauma/article/doi/10.1093/burnst/tkag007/8426274 by guest on 12 October 2026

Funding

This research was supported by the Key R&D plan of Shaanxi Province (number: 2024SF-YBXM−208).

Data availability

All the data are available in the main text or the Supplementary materials. The datasets generated and analyzed during the current study are available from the corresponding author upon reasonable request.

References

1. Bhardwaj H, Joshi R, Gupta A. Updated scenario on negative pressure wound therapy. *Int J Low Extrem Wounds* 2024;7:15347346241228788.
2. Yamashiro T, Kushibiki T, Mayumi Y, Tsuchiya M, Ishihara M, Azuma R. Negative-pressure wound therapy: what we know and what we need to know. *Adv Exp Med Biol* 2023;**1436**: 131–52.
3. Glass GE, Murphy GF, Esmaeili A, Lai LM, Nanchahal J. Systematic review of molecular mechanism of action of negative-pressure wound therapy. *Br J Surg* 2014;**101**:1627–36.
4. Ravindhran B, Schafer N, Howitt A, Carradice D, Smith G, Chetter I. Molecular mechanisms of action of negative pressure wound therapy: a systematic review. *Expert Rev Mol Med* 2023; **19**:e29.
5. Shou K, Niu Y, Zheng X, Ma Z, Jian C, Qi B. *et al.* Enhancement of bone-marrow-derived mesenchymal stem cell angiogenic capacity by NPWT for a combinatorial therapy to promote wound healing with large defect. *Biomed Res Int* 2017;**2017**:7920265.
6. Pandit V, Nesbitt SR, Kim DY, Mixon A, Kotha SP. Combinatorial therapy using negative pressure and varying lithium dosage for accelerated wound healing. *J Mech Behav Biomed Mater* 2015;**44**: 173–8.
7. Khalifa MO, Moriwaki T, Zhang S, Zhou W, Ito K, Li TS. Negative pressure induces dedifferentiation of hepatocytes via RhoA/ROCK pathway. *Biochem Biophys Res Commun* 2023;**30**:104–10.
8. Dong J, Qing C, Song F, Wang X, Lu S, Tian M. Potential molecular mechanisms of negative pressure in promoting wound healing. *Int Wound J* 2020;**17**:1428–38.
9. Yamashiro T, Kushibiki T, Mayumi Y, Tsuchiya M, Ishihara M, Azuma R. Novel cell culture system for monitoring cells during continuous and variable negative-pressure wound therapy. *Skin Res Technol* 2023;**29**:e13262.
10. Smit TH. Finite element models of osteocytes and their load-induced activation. *Curr Osteoporos Rep* 2022;**20**:127–40.
11. Jakka VVSV, Bursa J. Finite element simulations of mechanical behaviour of endothelial cells. *Biomed Res Int* 2021;**16**:8847372.
12. Chen X, Li J, Li Q, Zhang W, Lei Z, Qin D. *et al.* Spatial-temporal changes of mechanical microenvironment in skin wounds during negative pressure wound therapy. *ACS Biomater Sci Eng* 2019;**5**: 1762–70.
13. Cao R, Tian H, Tian Y, Fu X. A hierarchical Mechanotransduction system: from macro to micro. *Adv Sci (Weinh)* 2024;**11**: e2302327.
14. Jin J, Pan BH, Wang KA, Yu SS, Wu GS, Fang H. *et al.* Subvacuum environment-enhanced cell migration promotes wound healing without increasing hypertrophic scars caused by excessive cell proliferation. *Cell Prolif* 2023;**56**:e13493.
15. Baldwin C, Potter M, Clayton E, Irvine L, Dye J. Topical negative pressure stimulates endothelial migration and proliferation: a suggested mechanism for improved integration of integra. *Ann Plast Surg* 2009;**62**:92–6.
16. Wilkes RP, McNulty AK, Feeley TD, Schmidt MA, Kieswetter K. Bioreactor for application of subatmospheric pressure to three-dimensional cell culture. *Tissue Eng* 2007;**13**:3003–10.
17. McNulty AK, Schmidt M, Feeley T, Kieswetter K. Effects of negative pressure wound therapy on fibroblast viability, chemotactic signaling, and proliferation in a provisional wound (fibrin) matrix. *Wound Repair Regen* 2007;**15**:838–46.
18. McNulty AK, Schmidt M, Feeley T, Villanueva P, Kieswetter K. Effects of negative pressure wound therapy on cellular energetics in fibroblasts grown in a provisional wound (fibrin) matrix. *Wound Repair Regen* 2009;**17**:192–9.
19. Lu F, Ogawa R, Nguyen DT, Chen B, Guo D, Helm DL. *et al.* Microdeformation of three-dimensional cultured fibroblasts induces gene expression and morphological changes. *Ann Plast Surg* 2011;**66**:296–300.
20. Knoedler S, Broichhausen S, Guo R, Dai R, Knoedler L, Kauke-Navarro M. *et al.* Fibroblasts - the cellular choreographers of wound healing. *Front Immunol* 2023;**14**:1233800.
21. Peña OA, Martin P. Cellular and molecular mechanisms of skin wound healing. *Nat Rev Mol Cell Biol* 2024;**25**:599–616.
22. Ji S, Liu X, Huang J, Bao J, Chen Z, Han C. *et al.* Consensus on the application of negative pressure wound therapy of diabetic foot wounds. Burns. *Trauma.* 2021;**21**:tkab018.
23. Orsini EM, Perelas A, Southern BD, Grove LM, Olman MA, Scheraga RG. Stretching the function of innate immune cells. *Front Immunol* 2021;**2**:767319.
24. Chen G, Gao X, Chen J, Peng L, Chen S, Tang C. *et al.* Actomyosin activity and Piezo1 activity synergistically drive urinary system fibroblast activation. *Adv Sci (Weinh)* 2023;**10**:e2303369.
25. He J, Fang B, Shan S, Xie Y, Wang C, Zhang Y. *et al.* Mechanical stretch promotes hypertrophic scar formation through mechanically activated cation channel Piezo1. *Cell Death Dis* 2021; **12**:226.
26. Taivanbat B, Yamazaki S, Nasanbat B, Uchiyama A, Amalia SN, Nasan-Ochir M. *et al.* Transient receptor potential vanilloid 4 promotes cutaneous wound healing by regulating keratinocytes and fibroblasts migration and collagen production in fibroblasts in a mouse model. *J Dermatol Sci Netherlands* 2023;**112**:54–62.
27. Manabe T, Park H, Minami T. Calcineurin-nuclear factor for activated T cells (NFAT) signaling in pathophysiology of wound healing. *Inflamm Regen* 2021;**41**:26.
28. Nemlander A, Ahonen J, Wiktorowicz K, von Willebrand E, Hekali R, Lalla M. *et al.* Effect of cyclosporine on wound healing. *Transplantation.* 1983;**36**:1–6.
29. Zhang S, Xie Y, Yan F, Zhang Y, Yang Z, Chen Z. *et al.* Negative pressure wound therapy improves bone regeneration by promoting osteogenic differentiation via the AMPK-ULK1-autophagy axis. *Autophagy.* 2022;**18**:2229–45.
30. Hsu CC, Tsai WC, Chen CPC, Lu YM, Wang JS. Effects of negative pressures on epithelial tight junctions and migration in wound healing. *Am J Physiol Cell Physiol* 2010;**299**:C528–34.
31. Apelqvist J, Willy C, Fagerdahl A-M, Fraccalvieri M, Malmsjö M, Piaggesi A. *et al.* EWMA document: negative pressure wound therapy. *J Wound Care England* 2017;**26**:S1–154.
32. Formosa M, Ebejer SJ. Prophylactic negative pressure wound therapy in reducing surgical site infections: an evidence-based literature review. *SAGE Open Nurs United States* 2024;**10**:23779608241292840.
33. Eid ES, Kurban MS. A Piez-o the jigsaw: the Piezo1 channel in skin biology. *Clin Exp Dermatol* 2022;**47**:1036–47.
34. Holt JR, Zeng WZ, Evans EL, Woo SH, Ma S, Abuwarda H. *et al.* Spatiotemporal dynamics of PIEZO1 localization controls keratinocyte migration during wound healing. *Elife.* 2021;**27**:e65415.
35. Kang H, Hong Z, Zhong M, Klomp J, Bayless KJ, Mehta D. *et al.* Piezo1 mediates angiogenesis through activation of MT1-MMP signaling. *Am J Physiol Cell Physiol* 2019;**316**:C92–103.
36. Zhu H, He W, Ye P, Chen J, Wu X, Mu X. *et al.* Piezo1 in skin wound healing and related diseases: Mechanotransduction and therapeutic implications. *Int Immunopharmacol* 2023;**123**:110779.

Downloaded from academic.oup.com/burnstrauma/article/doi/10.1093/burnst/tkag007/8426274 by guest on 12 October 2026

37. Chen X, Wanggou S, Bodalia A, Zhu M, Dong W, Fan JJ. *et al*. A feedforward mechanism mediated by mechanosensitive Ion Channel PIEZO1 and tissue mechanics promotes glioma aggression. *Neuron*. 2018;**100**:799–815.e7.
38. Wang S, Cao S, Arhatte M, Li D, Shi Y, Kurz S. *et al*. Adipocyte Piezo1 mediates obesogenic adipogenesis through the FGF1/FGFR1 signaling pathway in mice. *Nat Commun* 2020;**11**:2303.
39. Hu Y, Tian H, Chen W, Liu Y, Cao Y, Pei H. *et al*. The critical role of the Piezo1/β-catenin/ATF4 Axis on the stemness of Gli1+ BMSCs during simulated microgravity-induced bone loss. *Adv Sci (Weinh)*. 2023;**10**:e2303375.
40. Davis J, Burr AR, Davis GF, Birnbaumer L, Molkentin JD. A TRPC6-dependent pathway for myofibroblast transdifferentiation and wound healing in vivo. *Dev Cell* 2012;**23**: 705–15.
41. Bayat M, Asgari-Moghadam Z, Maroufi M, Rezaie FS, Bayat M, Rakhshan M. Experimental wound healing using microamperage electrical stimulation in rabbits. *J Rehabil Res Dev* 2006;**43**: 219–26.
42. Chen QQ, Zhang W, Chen XF, Bao YJ, Wang J, Zhu WZ. Electrical field stimulation induces cardiac fibroblast proliferation through the calcineurin-NFAT pathway. *Can J Physiol Pharmacol* 2012;**90**: 1611–22.

Downloaded from academic.oup.com/burnstrauma/article/doi/10.1093/burnst/tkag007/8426274 by guest on 12 October 2026

© The Author(s) 2026. Published by Oxford University Press. This is an Open Access article distributed under the terms of the Creative Commons Attribution-NonCommercial License (https://creativecommons.org/licenses/by-nc/4.0/), which permits non-commercial re-use, distribution, and reproduction in any medium, provided the original work is properly cited. For commercial re-use, please contact reprints@oup.com for reprints and translation rights for reprints. All other permissions can be obtained through our RightsLink service via the Permissions link on the article page on our site—for further information please contact journals.permissions@oup.com.
Burns & Trauma, 2026, 14, tkag007
https://doi.org/10.1093/burnst/tkag007
Research Article